deformation twinning in commercial purity titanium at room temperature

Steven J. Lainé & Kevin M. Knowles

Published online: 18 Jun 2015.

Submit your article to this journal

Article views: 226

View related articles

View Crossmark data

Taylor & Francis
Taylor & Francis Group

{11$\bar{2}$4} deformation twinning in commercial purity titanium at room temperature

Steven J. Lainé* and Kevin M. Knowles

Department of Materials Science and Metallurgy, Rolls-Royce University Technology Centre, University of Cambridge, 27 Charles Babbage Road, Cambridge CB3 0FS, UK

Definitive evidence from both electron backscattered diffraction and transmission electron microscopy is shown for the existence of {11$\bar{2}$4} twinning as a rare deformation twinning mode in coarse-grained commercial purity titanium after room temperature ballistic impact testing at 10^3 s^{-1}. Non-Schmid-based twin-type selection is demonstrated for {11$\bar{2}$4} and the conjugate {11$\bar{2}$2} deformation twinning modes in this material within grains where the *c*-axis is closely aligned to the loading direction. Limited Schmid-based twin variant selection is shown for {11$\bar{2}$4} and {11$\bar{2}$2} deformation twinning modes in this material. The occurrence of high area fractions of {11$\bar{2}$4} twinning has relevance for high strain rate plasticity modelling of grains of textured titanium, compressed parallel to their *c*-axes.

Keywords: electron backscattered diffraction (EBSD); high-speed deformation; titanium; transmission electron microscopy (TEM); twinning

1. Introduction

Titanium has been used extensively and successfully in the aerospace industry since the 1950s. It is therefore somewhat surprising that there is a noticeable lack of literature on the understanding of the relationship between high strain rate deformation, deformation twinning modes and the microscale mechanics during the deformation of titanium alloys [1,2]. There are four commonly observed deformation twinning modes in titanium: {10$\bar{1}$2}, {11$\bar{2}$1} and {11$\bar{2}$2}, which occur at room temperature, and {10$\bar{1}$1} which is reported above 400 °C. Experimental evidence is abundant for these four twinning modes [3–7]. In addition, there are two more deformation twinning modes that are less commonly reported: {11$\bar{2}$3} and {11$\bar{2}$4} [4,6,8–21]. However, the evidence for the unequivocal existence of these two deformation twinning modes is far less robust than for the four commonly observed twinning modes, to the extent that Christian and Mahajan [6] hypothesized that habit plane markings cited as an evidence for {11$\bar{2}$3} deformation twinning was instead evidence for 'rather complex double twinning modes'.

By comparison with the evidence for {11$\bar{2}$3} deformation twinning, the evidence for {11$\bar{2}$4} deformation twinning is far stronger. Nevertheless, reports of its occurrence

---

*Corresponding author. Email: sl655@cam.ac.uk

This article was originally published with errors. This version has been corrected. Please see Erratum (http://dx.doi.org/10.1080/14786435.2015.1065135).

to date rely on indirect observations from either habit plane markings [4,8,9,11,13] or limited electron backscattered diffraction (EBSD) [19,20,21]. The first report of $\{11\bar{2}4\}$ twinning as a possible twinning mode in titanium was a brief 'Research in Progress' report by Liu and Steinberg in 1952, who examined single crystal titanium flakes produced by fused salt electrolysis and reported twinning of these flakes at room temperature on $\{10\bar{1}2\}$, $\{11\bar{2}1\}$, $\{11\bar{2}2\}$, $\{11\bar{2}3\}$ and $\{11\bar{2}4\}$ while being handled [8]. A subsequent, more detailed, study by Rosi et al. in 1956 [9] using two-surface analysis of coarse-grained titanium single crystals subjected to uniaxial tension at −196 °C was able to establish that $\{11\bar{2}4\}$ deformation twinning was the dominant twinning mode at this temperature.

The majority of references to $\{11\bar{2}4\}$ twinning since the work of Rosi et al. refer to their work, and in doing so lend credence to the proposition that $\{11\bar{2}4\}$ twinning operates only at cryogenic temperatures [11,12,19,22,23]. However, there is a evidence to suggest that $\{11\bar{2}4\}$ twinning does not just operate at cryogenic temperatures. Paton and Backofen reported some isolated instances of $\{11\bar{2}4\}$ twinning at both room temperature and elevated temperatures during compressive loading of single crystals oriented with the c-axis parallel to the loading direction [4]. Mullins and Patchett reported $\{11\bar{2}4\}$ twinning in textured titanium sheet metal in uniaxial, plane strain and biaxial tension at room temperature [11], and Ishiyama and Hanada also reported $\{11\bar{2}4\}$ twinning at room temperature in similarly textured material subjected to biaxial tension [13]. More recently, using EBSD, Xu et al. have reported $\{11\bar{2}4\}$ twinning at room temperature during dynamic plastic deformation of cylinders of textured high purity α-titanium in which the c-axes of grains lay ~35° from the loading direction [19,21], and Qin et al. have reported $\{11\bar{2}4\}$ twinning at room temperature during compression in textured polycrystalline high purity titanium, where the c-axis was aligned with the loading direction [20]. Interestingly, in the work of Xu et al., it was found that the relatively rarely reported $\{11\bar{2}4\}$ twinning always occurred in grains in which there was also $\{11\bar{2}2\}$ twinning [19].

The crystallography of the five established twinning modes is summarized in Table 1, with $\{11\bar{2}3\}$ being omitted because of the lack of conclusive evidence for its existence in titanium. Our own independent calculations leading to the entries in Table 1 confirm that the twinning elements of h.c.p. twinning modes in table IV of Yoo [5] and table 3 of Christian and Mahajan [6] are correct. It is noteworthy from table IV of [5] and table 3 of [6] that the $\{11\bar{2}2\}$ and $\{11\bar{2}4\}$ twinning modes have the same twinning shear because these two modes are conjugate to one another, as for the conjugate Type I and Type II twinning modes in α-uranium [24,25].

However, the statement by both Yoo [5] and Christian and Mahajan [6] that $\{11\bar{2}4\}$ twins are 'tension' twins, i.e., their formation causes an extension along the c-axis, is incorrect; they are in fact 'compression' twins, as it is evident from a consideration of the geometry of $\{11\bar{2}2\}$ and $\{11\bar{2}4\}$ twinning shown in Figure 1. It is apparent from the diagrams in Figure 1 that the sense of the twinning shear in these conjugate twinning modes is in the same sense relative to the c-axis, both causing a contraction. Hence, just as for the conjugate Type I and Type II twinning modes in α-uranium [25], the two modes allow for very similar senses of shape change in addition to having identical twinning shears. Furthermore, it is evident that twinning mode descriptions given in table 1 of Arthey and Roberts [10] which have been reproduced in a number of papers [11,14,15,21] also have typographical errors. For example, the

Table 1. Crystallography of possible deformation twinning modes in CP titanium using standard nomenclature for the twin plane K_1, shear direction η_1, second undistorted plane K_2 and direction η_2 lying in K_2 and the plane of shear [5–7]. For each deformation twinning mode a specific K_1 is selected to emphasize the crystallographic relations between K_1, η_1, K_2 and η_2. q is the complexity of the shuffles required to ensure all atoms in the twin are carried into their final correct positions [5–7]. 'T' and 'C' refer to the nomenclature of tension (T) and compression twins (C), which define whether the shape change produced by the twinning mode causes extension or contraction along the c-axis, respectively [5,6].

Type	K_1	η_1	K_2	η_2	Misorientation angle/axis (for c/a = 1.588)	Shear magnitude $\vert S \vert$	q	Refs.
T	$(10\bar{1}2)$	$[\bar{1}011]$	$(10\bar{1}2)$	$[10\bar{1}1]$	$[11\bar{2}0]$ 85.03°	0.174	4	[5,6]
T	$(11\bar{2}1)$	$[\bar{1}\bar{1}26]$	(0001)	$[11\bar{2}3]$	$[10\bar{1}0]$ 34.96°	0.630	2	[5,6]
C[a]	$(11\bar{2}4)$	$[22\bar{4}3]$	$(11\bar{2}2)$	$[11\bar{2}3]$	$[10\bar{1}0]$ 76.89°	0.219	6	[5,6]
C	$(11\bar{2}2)$	$[11\bar{2}3]$	$(11\bar{2}4)$	$[22\bar{4}3]$	$[10\bar{1}0]$ 64.40°	0.219	6	[5,6]
C	$(10\bar{1}1)$	$[\bar{1}012]$	$(\bar{1}013)$	$[30\bar{3}2]$	$[11\bar{2}0]$ 57.22°	0.099	8	[5,6]

[a]$\{11\bar{2}4\}$ is a compression twinning mode despite the assertions by Yoo [5] and Christian and Mahajan [6] that it is a tension twinning mode. See the text for details.

$\{11\bar{2}2\}$ and $\{11\bar{2}4\}$ twinning modes in this table have different twinning shears, and the $\langle 11\bar{2}1 \rangle$ η_1 directions given for $K_1 = \{11\bar{2}4\}$ do not actually lie in any of these K_1 planes.

The experimental conditions used in polycrystalline titanium to generate $\{11\bar{2}4\}$ twinning involve either compressing along the c-axis or directions close to the c-axis [19–21] or applying a tensile stress at angles close to 90° from the c-axis [9], in agreement with that expected for the 'compressive' mode for $\{11\bar{2}4\}$ and with the twinning elements in Table 1 and Figure 1.

While compelling, evidence of the occurrence of $\{11\bar{2}4\}$ twinning in EBSD is indirect, in the sense that it is reliant on a correct interpretation of an angle/axis misorientation relationship. As Qin et al. [20] note, the misorientation they quote of 77° about $\langle 10\bar{1}0 \rangle$ for twinning between a $\{11\bar{2}4\}$ twin and the matrix within which it forms is very close to a misorientation that they quote of 78° about $\langle 10\bar{1}0 \rangle$ for twinning between different $\{11\bar{2}2\}$ twin variants formed in the same grain. Bao et al. [27] provide a more through description of the angle/axis misorientation relationship that can result from $\{11\bar{2}2\}$ twin variants. There are six $\{11\bar{2}2\}$ twin variants that result in a misorientation of 77.29° about $\langle 1\bar{8}70 \rangle$ [27]. Given the angular tolerances required for the interpretation of EBSD data and the limits imposed by the spatial resolution of the technique, there remains the possibility that the recent reports of $\{11\bar{2}4\}$ twinning are not definitive evidence for the occurrence of this twinning mode. $[8\bar{1}\bar{7}0]$ is close enough to $[10\bar{1}0]$ for it to be indexed as $[10\bar{1}0]$ by the EBSD software. There are examples of this ambiguity of interpretation in Qin et al. [20], such as in their figure 7 (a), where there are boundaries which have been partially indexed as a $\{11\bar{2}4\}$ twin boundary and also as a $\{11\bar{2}2\}$–$\{1\bar{2}12\}$ variant–variant pair boundary. There are no examples of complete deformation twin traces fully indexed unambiguously as $\{11\bar{2}4\}$ in the micrographs shown in their paper. Xu et al. [19,21] present much stronger evidence of $\{11\bar{2}4\}$ twinning. However, the twin traces are close to the step size of the EBSD scans, with a frequency of only 0.5% of all twin boundaries identified as being
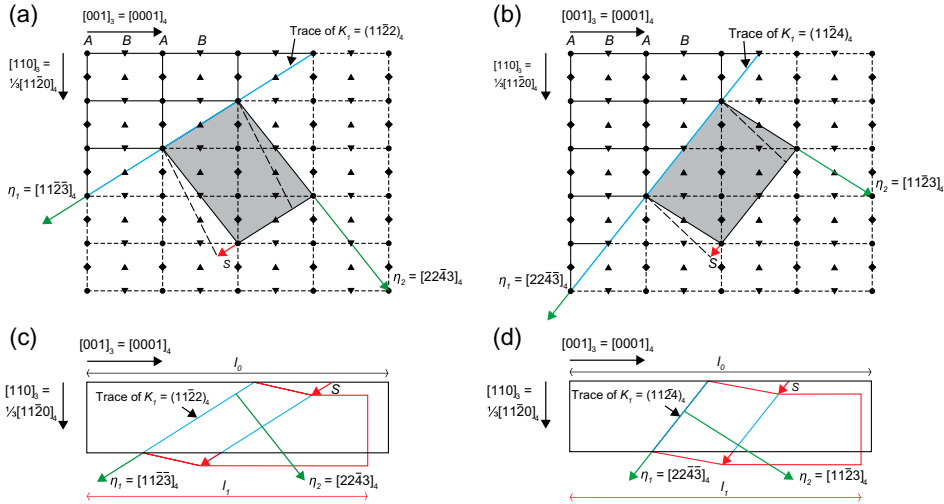
Figure 1. (colour online) Geometry of (a) $\{1\,1\,\bar{2}\,2\}$ and (b) $\{1\,1\,\bar{2}\,4\}$ twinning in a single crystal of titanium viewed normal to $(1\,0\,\bar{1}\,0)$. The composition plane K_1, twinning direction η_1, conjugate twinning direction η_2 and shear magnitude S are labelled. The shaded regions represent the super cell that undergoes the shear. The lattice point labelling system is that specified by Crocker and Bevis [26]. Using the *ABAB* stacking sequence designation of the h.c.p. crystal structure of α-titanium, the atom positions are represented by circles and squares for the *A* layer and triangles for the *B* layer. The atom positions displayed represent the projection of four $(1\,0\,\bar{1}\,0)$ planes: circles lie on the plane of the page, squares are one $(1\,0\,\bar{1}\,0)$ *d*-spacing below the page, upright triangles two $(1\,0\,\bar{1}\,0)$ *d*-spacings below the page and inverted triangles three $(1\,0\,\bar{1}\,0)$ *d*-spacings below the page. Representations of the macroscopic shape change to a single crystal of titanium deformed by twinning on $\{1\,1\,\bar{2}\,2\}$ and $\{1\,1\,\bar{2}\,4\}$ are shown in (c) and (d), respectively. It is evident that these twinning modes facilitate a macroscopic compression in line with the *c*-axis as in both cases; the pre-twinning crystal length l_0 is greater in magnitude than the post-twinning crystal length l_1.

$\{1\,1\,\bar{2}\,4\}$ twins. Furthermore, there is a clear example in figure 2(a) of Xu et al. [19], where a grain boundary is indexed incorrectly as $\{1\,1\,\bar{2}\,4\}$ twinning.

Here, we report conclusive evidence from a combination of both EBSD and transmission electron microscopy (TEM) for the existence of $\{1\,1\,\bar{2}\,4\}$ twinning as a rare deformation twinning mode in coarse-grained commercial purity (CP) titanium after room temperature ballistic impact testing. Under suitable circumstances, unprecedented area volume fractions of $\{1\,1\,\bar{2}\,4\}$ twinning are reported relative to prior work, with as much as 100% of twin boundaries in some suitably oriented grains being $\{1\,1\,\bar{2}\,4\}$ twin boundaries.

2. Experimental details

CP titanium Grade 1 with a coarse grain structure was selected for high strain rate deformation to investigate the deformation twinning modes that are activated. The desired as-received microstructure had been achieved by ageing the material in the high temperature β-phase field to promote grain growth, followed by a slow furnace cool. The approximate average prior β-grain diameter was 5.8 mm, assuming equiaxed β-grains. On cooling, each β-grain was colonized with an acicular microstructure of coarse α-platelets.

Table 2. CP titanium impurity levels for C, H, N and O determined from combustion analysis and for Fe determined from inductively coupled plasma optical emission spectrometry.

Element	C	Fe	H	N	O	Ti
Wt.%	0.037	0.027	0.0005	0.012	0.389	99.535

The α-platelets ranged in size from 30 to 200 μm, with an average width of 51 μm. The chemical composition of the CP titanium after heat treatment is shown in Table 2. It is apparent from this table that some oxygen uptake occurred during the heat treatment relative to the ASTM B265-13ae1 standard for Grade 1 CP titanium, in which the oxygen impurity level is specified to be no more than 0.18 wt% [28].

Ballistic tests were performed at room temperature at a strain rate of approximately 10^3 s^{-1}. A single-stage gas gun with a helium gas supply was used to propel cylindrical projectiles of the CP titanium at a hardened steel target at 250 ms^{-1}. The deformed cylinders were then sectioned longitudinally. Metallographic samples were prepared using the standard procedures for titanium [29]. Immersion etching of polished samples for 10 seconds in Keller's etch (1% HF, 1.5% HCl, 2.5% HNO_3, 95% H_2O by volume) highlighted their microstructure. A subsequent vibratory polish for 12 h in colloidal silica was used to prepare the samples for EBSD mapping. Focused ion beam (FIB) milling was used to extract TEM samples of specific areas of interest identified in the EBSD maps.

EBSD scans were conducted at either 20 or 25 kV using field emission gun (FEG) sources with either a CamScan MX2600 FEG scanning electron microscope (SEM) running the Oxford Instruments EBSD acquisition system, or a FEI Nova NanoSEM FEG running the Bruker EBSD acquisition system. The EBSD data were analysed using the *HKL Channel 5* software package distributed by Oxford Instruments and the *MTEX 4.0.9* toolbox for *Matlab*. TEM FIB samples were prepared using a FEI Helios Nano-Lab DualBeam FIB SEM and analysed using a JEOL 200CX transmission electron microscope at 200 kV equipped with a double tilt holder.

3. Results

During post-test analysis by optical microscopy, a grain was identified in which an individual large twin was surrounded by smaller twins with a different habit plane. An EBSD scan of the area confirmed the large twin had a misorientation between it and the surrounding matrix of approximately 77° about $[1\,0\,\overline{1}\,0]$ within experimental error. This area is shown in Figure 2(a), with the normal to the various parts of the grain shown in colours conforming to the inverse pole figure. The specific $\{1\,1\,\overline{2}\,4\}$ twin variant of the K_1 composition plane was calculated to be $(\overline{1}\,2\,\overline{1}\,4)$ from an analysis of the EBSD data. The predicted orientations for $\{1\,1\,\overline{2}\,4\}$ twin variants were calculated from the parent grain orientation following the procedure described by Jiang et al. [30]. Further verification of the twin variant was possible by comparing the measured misorientation between other twin types and twin variants in the same scan. For example, in Figure 2(a), the parent grain orientation is rotated to the potential $\{1\,1\,\overline{2}\,4\}$ twin orientations by applying an angle-axis rotation of 76.89° about the six $\langle 0\,1\,\overline{1}\,0 \rangle$ giving six possible orientations for the six variants of $\{1\,1\,\overline{2}\,4\}$. Of the six possible variants, the
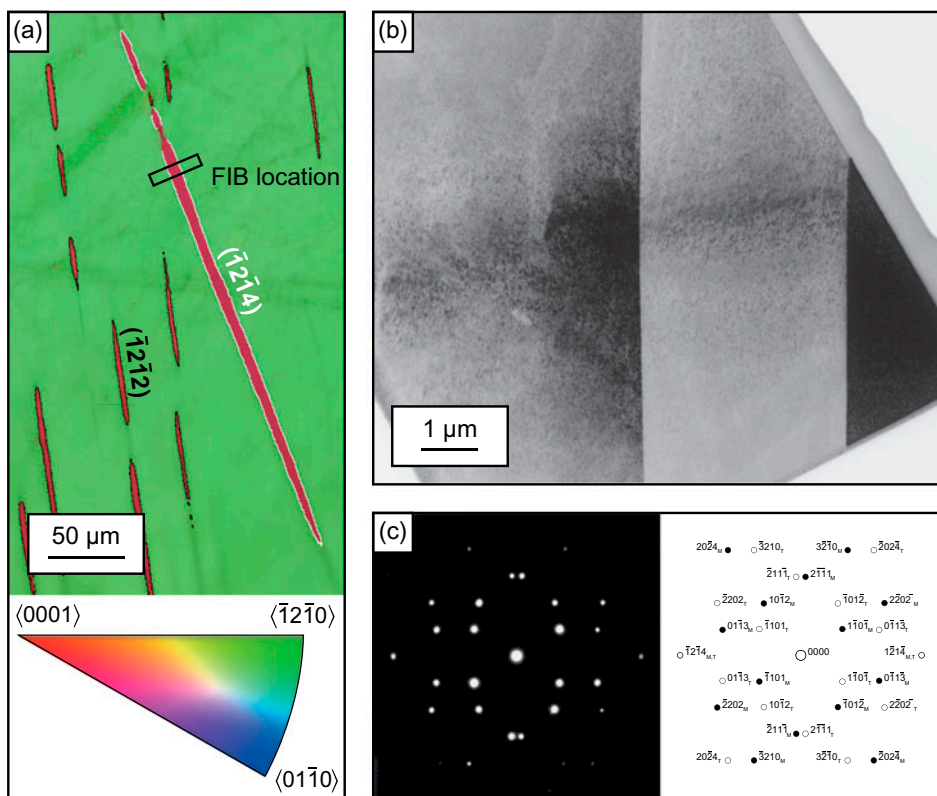
Figure 2. (colour online) (a) EBSD scan of an individual $\{1\,1\,\bar{2}\,4\}$ deformation twin and smaller $\{1\,1\,\bar{2}\,2\}$ twins acquired at 25 kV with a 0.5 μm step size, inverse pole figure colouring and band contrast, with the $\{1\,1\,\bar{2}\,4\}$ twin outlined in white and the smaller $\{1\,1\,\bar{2}\,2\}$ twins outlined in black. The loading direction is in the horizontal direction. (b) Bright field image of the TEM specimen taken from the boxed region in (a). (c) Electron diffraction pattern from (b) taken down the $[1\,4\,\bar{5}\,3]$ zone ($[2\,3\,\bar{1}]$ in the three index notation) common to both the matrix and the twin confirming twinning on $(\bar{1}\,2\,\bar{1}\,4)$. This electron diffraction pattern has been image processed to highlight the $\bar{1}\,2\,\bar{1}\,4$ and $1\,\bar{2}\,1\,\bar{4}$ twin spots, which have a low intensity because of their large $|\mathbf{g}|$.

$(\bar{1}\,2\,\bar{1}\,4)$ has a misorientation of 5.47° from the measured orientation for the $\{1\,1\,\bar{2}\,4\}$ twin. Similarly for the $\{1\,1\,\bar{2}\,2\}$ twins also seen in Figure 2(a), the $(\bar{1}\,2\,\bar{1}\,2)$ variant has a misorientation of 3.87° from the average measured orientation for the $\{1\,1\,\bar{2}\,2\}$ twins. In addition, the misorientation between the $(\bar{1}\,2\,\bar{1}\,4)$ twin and the $(\bar{1}\,2\,\bar{1}\,2)$ twins in Figure 2(a) was 13.54° which is very close to the calculated misorientation expected between a $(\bar{1}\,2\,\bar{1}\,4)$ twin and a $(\bar{1}\,2\,\bar{1}\,2)$ twin of 12.36°.

Careful FIB lift out and milling of the area highlighted in Figure 2(a) enabled TEM to be undertaken of this area. A low magnification bright field TEM image of the resulting thin foil is shown in Figure 2(b), in which the interface between the 3.5 μm thick twin and the surrounding matrix is parallel to the electron beam. The electron diffraction pattern in Figure 2(c) and its indexed schematic confirmed the $(\bar{1}\,2\,\bar{1}\,4)$ twin relationship between the large twin and the surrounding matrix for this $[1\,4\,\bar{5}\,3]$ zone ($[2\,3\,\bar{1}]$ in three index notation) common to both the matrix and the twin.

Other electron diffraction patterns are shown in Figure 3, found by tilting the specimen so the interface between the twin and matrix remained parallel to the electron
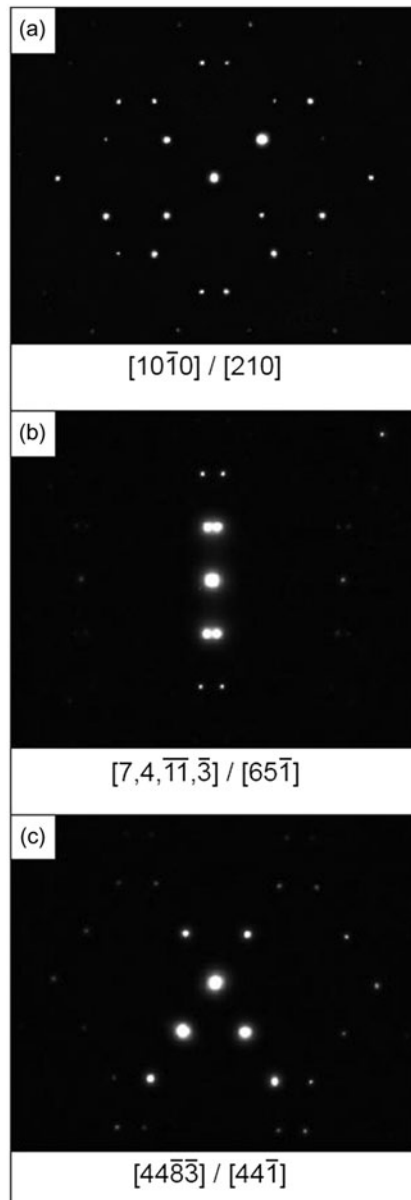
Figure 3. Electron diffraction patterns from Figure 2(b), (a) viewed down the $[10\bar{1}0]$ zone ($[2\,1\,0]$ in the three index notation) (b) viewed down the $[7,4,\bar{1}\bar{1},\bar{3}]$ zone ($[6\,5\,\bar{1}]$ in the three index notation) and (c) viewed down the $[44\bar{8}\bar{3}]$ zone ($[4\,4\,\bar{1}]$ in the three index notation) common to both the matrix and the twin confirming twinning on $(\bar{1}\,2\,\bar{1}\,4)$. As in Figure 2, the electron diffraction patterns have been image processed to highlight the $\bar{1}\,2\,\bar{1}\,4$ and $1\,\bar{2}\,1\,\bar{4}$ twin spots, which have a low intensity because of their large $|\mathbf{g}|$.

beam, were consistent with the expected angular relationships between the different zones, providing additional confirmation of this $(\bar{1}\,2\,\bar{1}\,4)$ twin relationship.

Further analysis of the ballistically tested samples in the light of this conclusive evidence for the presence of $\{1\,1\,\bar{2}\,4\}$ deformation twins showed that large numbers of these twins were present in grains in which the c-axis was aligned within 6° of the loading direction (Figure 4). Interestingly, the $\{1\,1\,\bar{2}\,4\}$ deformation twin shown in Figure 2 was particularly unusual because it was actually found in a grain in which the c-axis was 25° away from the cylinder compression direction. The area fractions of $\{1\,1\,\bar{2}\,4\}$ twins compared to $\{1\,1\,\bar{2}\,2\}$ twins in Figures 2(a) and 4(c)–(e) are summarized in Table 3.
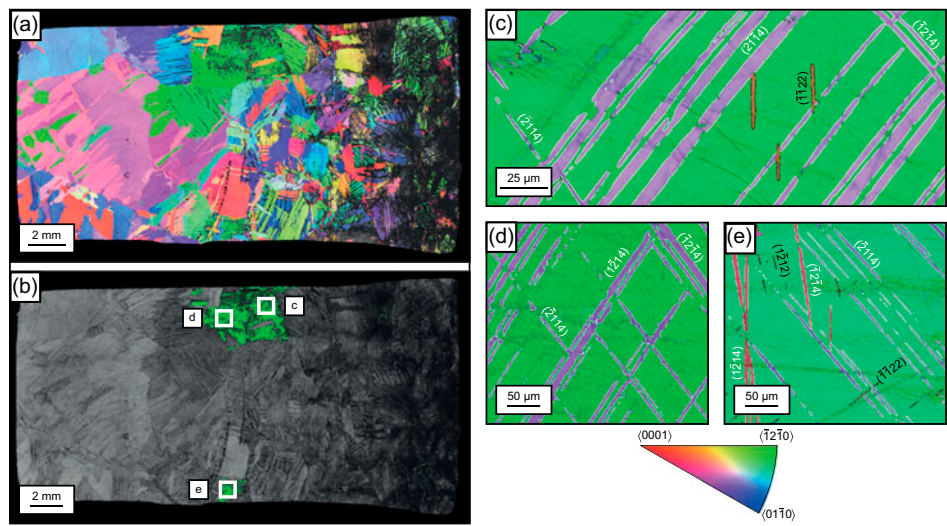

Figure 4. (colour online) (a) EBSD scan of an indi (a) EBSD scan of a longitudinally sectioned ballistically tested projectile acquired at 25 kV with a 15 μm step size, inverse pole figure colouring and band contrast. The loading direction is in the horizontal direction, with the impact face on the right-hand side. (b) Band contrast with grains whose c-axes were within 6° of the loading direction highlighted in green. (c)–(e) EBSD scans of the highlighted green grains in (b) acquired at 25 kV with a 0.5 μm step size, with inverse pole figure colouring and band contrast, showing large $\{1\,1\,\bar{2}\,4\}$ twins outlined in white and smaller $\{1\,1\,\bar{2}\,2\}$ twins outlined in black.

Table 3. Area fractions of deformation twins in Figures 2(a) and 4(c)–(e) as percentages of the EBSD scan area of a grain, and area percentage of twinned area for $\{1\,1\,\bar{2}\,4\}$ and $\{1\,1\,\bar{2}\,2\}$ deformation twins.

	Area fractions expressed as a percentage			
	Figure 2(a)	Figure 4(c)	Figure 4(d)	Figure 4(e)
Percentage of EBSD scan area $\{1\,1\,\bar{2}\,4\}$	2.5%	23.2%	17.8%	7.7%
Percentage of EBSD scan area $\{1\,1\,\bar{2}\,2\}$	2.2%	0.5%	0%	0.4%
Percentage of $\{1\,1\,\bar{2}\,4\}$ twins	53.1%	97.8%	100%	95.2%
Percentage of $\{1\,1\,\bar{2}\,2\}$ twins	46.9%	2.2%	0%	4.8%

4. Discussion

Variants of other families of deformation twins when they were present within the same grains as $\{11\bar{2}4\}$ compression twins were always of the conjugate $\{11\bar{2}2\}$ compression-type twinning. However, it is evident from Figure 4(d), it was not a requirement that $\{11\bar{2}4\}$ twins within a grain had to be accompanied by $\{11\bar{2}2\}$ twins. No $\{11\bar{2}4\}$ twins were observed in grains whose c-axis directions orientations deviated more than 30° from the compression direction. Hence, our observations are in agreement with those of Rosi et al. [9] who observed profuse $\{11\bar{2}4\}$ twinning in coarse-grained `-° away from [0 0 0 1]. They are also in good agreement with the observations of Xu et al. [19], except that in our work we have not found that $\{11\bar{2}4\}$ twins within a grain have always to be accompanied by $\{11\bar{2}2\}$ twins.

The presence of only $\{11\bar{2}4\}$ and $\{11\bar{2}2\}$ deformation twins in particular grains aligned with their c-axes close to the compression direction demonstrates non-Schmid dependent selection of the choice of deformation mode within a grain (Table 4). Considering that the loading direction with the c-axis is in compression, it is logical to expect only compressive twinning modes. Therefore, on this basis, twinning on $\{10\bar{1}2\}$ and $\{10\bar{2}1\}$ for the grains shown in Figures 2(a) and 4(c)–(e) can be disregarded.

For the grain shown in Figure 2(a), twinning on one of the six possible $\{10\bar{1}1\}$ actually had the highest Schmid factor, even though $\{11\bar{2}2\}$ and $\{11\bar{2}4\}$ twinning was observed. Intriguingly, no evidence was found for $\{10\bar{1}1\}$ twinning in the entire sample. In Figure 4(c)–(e), variants from the $\{11\bar{2}4\}$ deformation twinning modes actually had the highest Schmid factors. The dominant twinning mode in these grains was $\{11\bar{2}4\}$, consistent with what might therefore be expected. By comparison with twinning on $\{11\bar{2}2\}$ and $\{11\bar{2}4\}$, $\{10\bar{1}1\}$ had a significant Schmid factor in Figure 4(c)–(e). We also observed that even when $\{11\bar{2}4\}$ deformation twinning alone was found in a particular grain, as in Figure 4(d), grains adjacent to such a grain showed $\{11\bar{2}2\}$ deformation twinning, again emphasising the close relationship between these conjugate twinning modes.

Having indexed the deformation twin variants present within each deformation twin-type using the procedure of Jiang et al. [30], it was possible to evaluate the Schmid factors for the individual variants in Figures 2(a) and 4(c)–(e). These are shown in Table 5. In Figure 2(a), $(\bar{1}2\bar{1}2)$, the active $\{11\bar{2}2\}$ twinning variant, had the highest Schmid factor out of the possible $\{11\bar{2}2\}$ variants. However, $(\bar{1}2\bar{1}4)$, the active $\{11\bar{2}4\}$ twin variant had the lowest Schmid factor out of the possible $\{11\bar{2}4\}$ variants, which

Table 4. Highest Schmid factors for twinning within each possible deformation twinning mode for the grains shown in Figures 2(a) and 4(c)–(e), assuming plane strain compression loading in the x-direction which is horizontal across the page in each of these figures, compressing the crystal c-axis.

	Highest Schmid factor, x-direction, plane strain			
Deformation twin mode	Figure 2(a)	Figure 4(c)	Figure 4(d)	Figure 4(e)
$\{11\bar{2}4\}$	**0.399**	**0.498**	**0.500**	**0.497**
$\{11\bar{2}2\}$	**0.443**	**0.477**	0.485	**0.474**
$\{10\bar{1}1\}$	0.468	0.452	0.462	0.449

Note: The operative twinning modes are in bold.

confirms observations by Jiang et al. that second twinning variants or twinning types cannot be reliably predicted by Schmid factors [30]. The non-Schmid-based variant selection suggests that there were additional factors contributing to the isolated occurrence of $\{11\bar{2}4\}$ deformation twinning in Figure 2(a). It is plausible that changes to the local stress state by $\{11\bar{2}2\}$ deformation twinning preceding the nucleation of the $\{11\bar{2}4\}$ deformation twin had meant that the local resolved loading direction was significantly different to the macroscopic loading direction to initiate this $\{11\bar{2}4\}$ deformation twin. Schmid-based twinning variant selection is often reported in h.c.p. materials [19,27, 31–33]. However, non-Schmid-based variant selection can be triggered for a number of reasons when the macroscopic loading configuration differs significantly from the local stress state. For example evidence has been presented by others that the local stress state may be different because of complex local stress states in polycrystalline materials [34,35], 'accommodation strain' in neighbouring grains [36,37], or nonuniform stresses arising from dislocations or residual stresses [34].

In Figure 4(c)–(e), the loading direction is more closely aligned to the *c*-axis so the Schmid factors do not vary as much for the $\{11\bar{2}4\}$ and $\{11\bar{2}2\}$ variants as in Figure 2(a), but again the Schmid factors did not accurately predict the active variants. Although, the $\{11\bar{2}4\}$ twin variants with the highest Schmid factor in Figure 4(c) and 4(d) were operative, $(2\bar{1}\bar{1}4)$ and $(1\bar{2}14)$, respectively, the remaining operative twin variants did not follow from the Schmid criterion, as is apparent from Table 5.

Clearly, if there is less spread in the Schmid factor magnitudes then there is less to discriminate between different variants. The similarity in the Schmid factor values in Figure 4(c)–(e) for $\{11\bar{2}4\}$ twin variants is likely to have contributed to the high number of different $\{11\bar{2}4\}$ variants being operative in each grain. This similarity in the Schmid factors can be demonstrated graphically. In Figure 5(a) and 5(b), the variation of positive Schmid factors for loading in compression is demonstrated for twinning on $\{11\bar{2}4\}$; the position where the Schmid factor is at a maximum of 0.5 is 6.5° away

Table 5. Schmid factors for the six $\{11\bar{2}4\}$ and $\{11\bar{2}2\}$ deformation twin variants for the grains shown in Figures 2(a) and 4(c)–(e), assuming plane strain compression loading in the *x*-direction which is horizontal across the page in each of these figures, compressing the crystal *c*-axis.

	Schmid factor, *x*-direction plane strain			
Deformation twin variant	Figure 2(a)	Figure 4(c)	Figure 4(d)	Figure 4(e)
$\{11\bar{2}4\}$ V1: $(11\bar{2}4)$	0.377	0.493	0.472	0.494
$\{11\bar{2}4\}$ V2: $(\bar{1}2\bar{1}4)$	**0.223**	**0.478**	**0.455**	**0.481**
$\{11\bar{2}4\}$ V3: $(\bar{2}114)$	0.253	**0.466**	**0.467**	**0.469**
$\{11\bar{2}4\}$ V4: $(\bar{1}\bar{1}24)$	0.398	0.474	0.490	0.475
$\{11\bar{2}4\}$ V5: $(1\bar{2}14)$	0.390	0.490	**0.500**	**0.489**
$\{11\bar{2}4\}$ V6: $(2\bar{1}\bar{1}4)$	0.399	**0.498**	0.494	0.497
$\{11\bar{2}2\}$ V1: $(11\bar{2}2)$	0.379	0.430	0.463	0.431
$\{11\bar{2}2\}$ V2: $(\bar{1}2\bar{1}2)$	**0.443**	0.461	0.485	0.457
$\{11\bar{2}2\}$ V3: $(\bar{2}112)$	0.441	0.477	0.470	0.474
$\{11\bar{2}2\}$ V4: $(\bar{1}\bar{1}22)$	0.339	**0.466**	0.428	**0.467**
$\{11\bar{2}2\}$ V5: $(1\bar{2}12)$	0.126	0.436	0.399	**0.441**
$\{11\bar{2}2\}$ V6: $(2\bar{1}\bar{1}2)$	0.163	0.416	0.420	0.422

Note: The operative twinning modes are in bold.

from $[0\,0\,0\,1]$ and 45° from the $\{1\,1\,\bar{2}\,4\}$ pole. For twinning on any of the possible $\{1\,1\,\bar{2}\,4\}$ twin variants, the Schmid factor plots of Figure 5(c) and 5(d) are relevant; these show the maximum Schmid factor as a function of location of the compression axis and demonstrate the principle that for compression axes within ~12° of $[0\,0\,0\,1]$, it is highly likely that there will be at least one $\{1\,1\,\bar{2}\,4\}$ twin variant with a Schmid factor very close to 0.5.

A final consideration is the complete absence of any $\{1\,0\,\bar{1}\,1\}$ twinning in the ballistically tested specimen. Since twinning on $\{1\,0\,\bar{1}\,1\}$ in the absence of any other plastic deformation process causes a contraction parallel to the *c*-axis, it might be reasonably assumed that this deformation twinning mode might be favoured in room temperature ballistic testing. However, $\{1\,0\,\bar{1}\,1\}$ twinning has a complex shuffle mechanism [6], and it is this which would seem to preclude it as an observed deformation twinning mode at room temperature, even at a strain rate of 10^3 s^{-1} and under conditions where rare $\{1\,1\,\bar{2}\,4\}$ compression-type twins are activated. This is also consistent
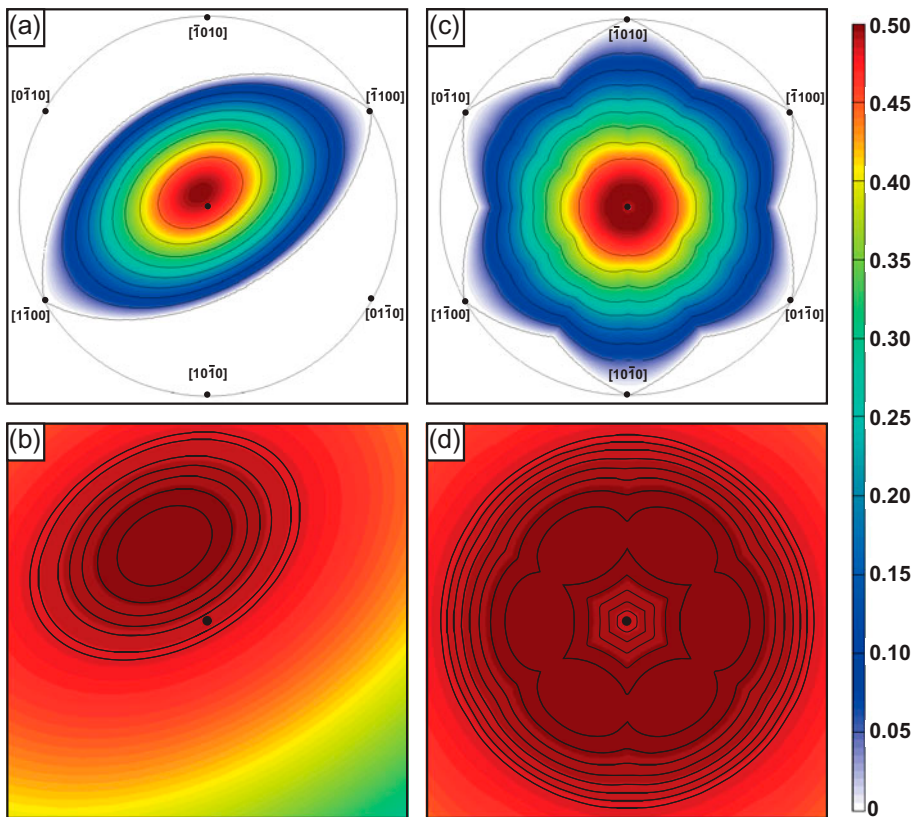

Figure 5. (colour online) (a) and (b) The variation of positive Schmid factors for loading in compression for twinning on $\{1\,1\,\bar{2}\,4\}$; the position where the Schmid factor is at a maximum of 0.5 is 6.5° away from $[0\,0\,0\,1]$ and 45° from the $(1\,1\,\bar{2}\,4)$ pole. (c) and (d) Maximum positive Schmid factors for loading in compression for twinning on $\{1\,1\,\bar{2}\,4\}$. In (a)–(d) the $[0\,0\,0\,1]$ pole is indicated by a black dot.

with the observations of Xu et al. [19], who found evidence from EBSD of occasional $\{1\,1\,\bar{2}\,4\}$ twinning, but no $\{1\,0\,\bar{1}\,1\}$ twinning, at strain rates of 4.5–5 $\times 10^2$ s^{-1} [19].

5. Conclusions

Conclusive and definitive evidence has been found for regions of $\{1\,1\,\bar{2}\,4\}$ deformation twinning in CP titanium ballistically tested at room temperature. Our results also confirm the link between $\{1\,1\,\bar{2}\,4\}$ and $\{1\,1\,\bar{2}\,2\}$ deformation twinning found by Xu et al. [19]. Although, the observation that $\{1\,1\,\bar{2}\,4\}$ twinning occurs when the *c*-axis is loaded in compression is consistent with previous research by Rosi et al. [8] and Xu et al. [19], the high area fraction of $\{1\,1\,\bar{2}\,4\}$ we have found in particular grains is unprecedented. This is relevant for plasticity modelling and deformation twin modelling of high strain rate events in heavily textured materials where there is a strong [0 0 0 1] fibre texture aligned with the loading direction. CP titanium can exhibit a strong [0 0 0 1] fibre texture perpendicular to the extrusion axis in extruded bars [38], and normal to the rolling direction if forged and then cross-rolled to a 1.75 von Mises equivalent strain [39]. By contrast, the lack of observations of $\{1\,0\,\bar{1}\,1\}$ twinning calls into question whether this can be considered as a possible mode of deformation in titanium subjected at room temperature to strain rates $> 5 \times 10^2$ s^{-1}.

When more than one deformation twin variant or deformation twin-type is present within a specific grain, our results show that the Schmid criterion is a poor predictor of deformation twin variants at high strain rates at room temperature. Instead, in order to predict the deformation twin variants with some degree of confidence, it will be necessary to model the local stress state in each grain incrementally with time as new deformation twins nucleate.

Disclosure statement

No potential conflict of interest was reported by the authors.

ORCID

Steven J. Lainé http://orcid.org/0000-0003-0220-3330

References

[1] S.L. Raghunathan, R.J. Talling and D. Dye, J. Strain Anal. Eng. Des. 45 (2010) p.337.
[2] F. Coghe, W. Tirry, L. Rabet, D. Schryvers and P. Van Houtte, Mater. Sci. Eng. A 537 (2012) p.1.
[3] F.D. Rosi, C.A. Dube and B.H. Alexander, Trans. Am. Inst. Min. Eng. 197 (1953) p.257.
[4] N.E. Paton and W.A. Backofen, Metall. Trans. 1 (1970) p.2839.
[5] M.H. Yoo, Metall. Trans. A 12 (1981) p.409.
[6] J.W. Christian and S. Mahajan, Prog. Mater. Sci. 39 (1995) p.1.
[7] A. Kelly and K.M. Knowles, *Crystallography and Crystal Defects*, 2nd ed., John Wiley & Sons Ltd, Chichester, 2012.
[8] T.S. Liu and M.A. Steinberg, Trans. Am. Inst. Min. Eng. 194 (1952) p.1043.
[9] F.D. Rosi, F.C. Perkins and L.L. Seigle, Trans. Am. Inst. Min. Eng. 206 (1956) p.115.
[10] R.P. Arthey and W.T. Roberts, Met. Technol. 3 (1976) p.317.
[11] S. Mullins and B.M. Patchett, Metall. Trans. A 12 (1981) p.853.
[12] S. Ishiyama, S. Hanada and O. Izumi, J. Japan Inst. Met. 54 (1990) p.976.
[13] S. Ishiyama and S. Hanada, J. Japan Inst. Met. 55 (1991) p.1315.
[14] H.C. Gu, H.F. Guo, S.F. Chang and C. Laird, Mater. Sci. Eng. A 188 (1994) p.23.
[15] X.L. Tan, H.C. Gu, S.F. Zhang and C. Laird, Mater. Sci. Eng. A 189 (1994) p.77.
[16] X.L. Tan, H.C. Gu and Z.G. Wang, Mater. Sci. Eng. A 196 (1995) p.45.
[17] X. Tan, H. Gu, C. Laird and N.D.H. Munroe, Metall. Mater. Trans. A 29 (1998) p.507.
[18] Z.F. Zhang, H.C. Gu and X.L. Tan, J. Mater. Sci. Lett. 17 (1998) p.211.
[19] F. Xu, X.Y. Zhang, H.T. Ni and Q. Liu, Mater. Sci. Eng. A 541 (2012) p.190.
[20] H. Qin, J.J. Jonas, H.B. Yu, N. Brodusch, R. Gauvin and X.Y. Zhang, Acta Mater. 71 (2014) p.293.
[21] F. Xu, X.Y. Zhang, H.T. Ni, Y.M. Cheng, Y.T. Zhu and Q. Liu, Mater. Sci. Eng. A 564 (2012) p.22.
[22] N.M. Madhava and R.W. Armstrong, Metall. Trans. 5 (1974) p.1517.
[23] R.G. Broadwell and C.F. Hickey, *Toughness and Fracture Behavior of Titanium*, ASTM STP 651, American Society for Testing and Materials, Philadelphia, 1978.
[24] R.W. Cahn, Acta Metall. 1 (1953) p.49.
[25] R.J. McCabe, L. Capolungo, P.E. Marshall, C.M. Cady and C.N. Tomé, Acta Mater. 58 (2010) p.5447.
[26] A.G. Crocker and M. Bevis, Deformation and Fracture, in *The Science, Technology and Application of Titanium*, R.I. Jaffee and N.E. Promisel, eds., Pergamon Press, Oxford, 1970, p.453.
[27] L. Bao, C. Schuman, J.-S. Lecomte, Z. Zhang, M.-J. Philippe, X. Zhao and C. Esling, Adv. Eng. Mater. 13 (2011) p.928.
[28] ASTM Standard B265-13ae1, *Standard Specification for Titanium and Titanium Alloy Strip, Sheet and Plate*, ASTM International, West Conshohocken, 2013.
[29] W.L. Finlay, J. Resketo and M.B. Vordahl, Ind. Eng. Chem. 42 (1950) p.218.
[30] J. Jiang, A. Godfrey, W. Liu and Q. Liu, Scr. Mater. 58 (2008) p.122.
[31] S. Godet, L. Jiang, A.A. Luo and J. Jonas, Scr. Mater. 55 (2006) p.1055.
[32] S.H. Park, S.-G. Hong and C.S. Lee, Scr. Mater. 62 (2010) p.202.
[33] X.G. Deng, S.X. Hui, W.J. Ye and X.Y. Song, Mater. Sci. Eng. A. 575 (2013) p.15.
[34] I.J. Beyerlein, L. Capolungo, P.E. Marshall, R.J. McCabe and C.N. Tomé, Philos. Mag. 90 (2010) p.2161.
[35] A. Fernández, A. Jérusalem, I. Gutiérrez-Urrutia and M.T. Pérez-Prado, Acta Mater. 61 (2013) p.7679.
[36] J.J. Jonas, S. Mu, T. Al-Samman, G. Gottstein, L. Jiang and É. Martin, Acta Mater. 59 (2011) p.2046.

[37] S. Mu, J.J. Jonas and G. Gottstein, Acta Mater. 60 (2012) p.2043.
[38] I.L. Dillamore and W.T. Roberts, Metall. Rev. 10 (1965) p.271.
[39] U.F. Kocks, C.N. Tomé and H.-R. Wenk, *Texture and Anisotropy: Preferred Orientation in Polycrystals and Their Effect on Materials Properties*, Cambridge University Press, Cambridge, 1998.